Vol. 31 (2000) *ACTA PHYSICA POLONICA B* No 12

ELECTRON CORRELATION EFFECTS IN $NiS_{2-x}Se_x$ AND V_2O_3*

J.M. Honig

Department of Chemistry, Purdue University
West Lafayette, IN 47907-1393, USA

(Received November 7, 2000)

In this article we discuss two manifestations of electron correlation effects, namely the electrical characteristics and quantum critical phenomena observed in the $NiS_{2-x}Se_x$ system, and the electrical properties and orbital ordering effects encountered in the V_2O_3 system. Considerable emphasis will be placed on recent developments.

PACS numbers: 71.30.+h, 71.28.+d, 72.80.Ga

1. The $NiS_{2-x}Se_x$ system

The $NiS_{2-x}Se_x$ system represents one of the rare cases for which it is possible completely to alter the electronic properties of the compound by fine-tuning the anion composition, in this case, the S/Se ratio. The end member NiS_2 is a semiconductor (or insulator as temperature $T \to 0$), whereas $NiSe_2$ is a poor metal. These compounds can be mixed in all proportions without changing the cubic pyrite structure; the lattice parameter varies linearly with x in accord with Vegard's law. Clearly, at some intermediate composition the system must progress from one electronic state to the other — leading to interesting physical consequences. The $NiS_{2-x}Se_x$ system presents the additional advantage that the gradation of physical properties is achieved by isoelectronic substitution in the anion sublattice, while leaving the cationic sublattice intact and the electron count constant. This is to be contrasted with almost all comparable systems in which the alteration of electronic properties is achieved by aliovalent substitutions of ions in the cation sublattice: this process produces cation vacancies, changes in the electron density, and is also generally associated with changes in lattice symmetry — complications that one normally wishes to avoid.

---

[*] Presented at the XL Cracow School of Theoretical Physics, Zakopane, Poland June 3–11, 2000.

The physical properties of the $NiS_{2-x}Se_x$ system as studied by numerous workers have been extensively reviewed in a recent article [1] and will not again be discussed in detail. We thus concentrate on recent studies in which the author has participated. The relevant electrical properties are summarized as sketched below: *(i)* In the composition range $0 \leq x \leq 0.3$ the material displays insulating characteristics depicted in Fig. 1(a). From plots of $\log \rho$ *vs* $1/T$ (ρ is the resistivity, T the temperature) one deduces energy gaps of ca. 220 meV at higher and 660 meV at lower temperatures, where the system is in the Paramagnetic Insulating (PI) and canted AntiFerromagnetic Insulating (AFI) regimes, respectively. The increase in gap size presumable arises from the Slater mechanism for the prevailing canted AF order. *(ii)* In the range $0.38 \leq x \leq 0.51$ the resistivity displays metallic characteristics at low T; this is followed by a very steep rise in ρ with T, due to the gradual opening of a band gap. Beyond the maximum in ρ the alloy exhibits semiconducting characteristics, with a band gap of 220 meV. These properties are sketched in Fig. 1(b); the size of the hump diminishes with increasing x. *(iii)* For $x \geq 0.55$ the material is a poor metal, as depicted in Fig. 1(c).

The Seebeck coefficients α in these three composition ranges also display unusual properties; *cf.* Figs. 1(d), 1(e), 1(f). In regime *(i)* α is almost exactly zero at low T, precisely in the range where ρ rises sharply and indefinitely with diminishing temperature; α then passes through a very large maximum at intermediate T and finally drops off again. These results go counter the general rule that the variation of α with T should qualitatively mimic that of ρ with T. In regime *(ii)* the size of the maximum is considerably suppressed. In regime *(iii)* α is slightly negative, numerically very small, and linear in T. These latter results are in conformity with standard theories of the Seebeck coefficients of metals [2].

The above findings may be rationalized by the qualitative band structure diagram of Fig. 2. The important features involve the band of primarily cationic $3e_g$ character, with some anionic admixture; this band is rather narrow and is half-filled, as shown in Fig. 2(a). In relatively recent theoretical studies [3] involving electron correlation effects in crystals of infinite dimensionality it has been established that the Mott–Hubbard picture of the Metal–Insulator Transition (MIT) must be modified. In the more recent theories there is no collapse of the band gap separating the upper and lower Hubbard subbands when a correlated electron system undergoes the MIT. Instead, the density of states (DOS) pattern shifts such that for the metallic state a central peak develops in the DOS around the Fermi level ε_F, at the expense of states in the two Hubbard subbands. This gives rise to the undulating characteristics of the DOS for the e_g band sketched in Fig. 2(a). A wide S–Se $3p\sigma$–$4p\sigma$ band with some cationic admixture is energetically situ-

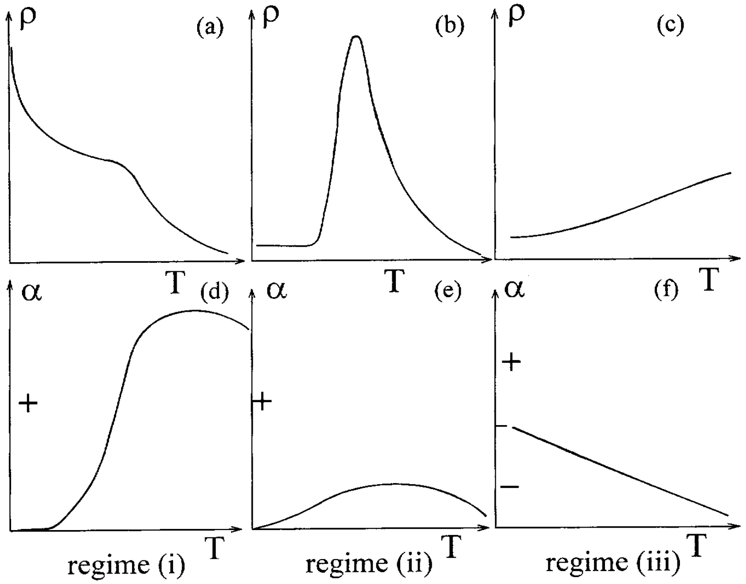

Fig. 1. Schematic diagram of the electrical properties of $NiS_{2-x}Se_x$ below 300 K. Resistivity ρ *vs* temperature T for $0 \leq x \leq 0.30$ (part (a)), $0.38 \leq x \leq 0.52$ (part (b)), and $x > 0.55$ (part (c)). Seebeck coefficient α *vs* T for $0 \leq x \leq 0.30$ (part (d)), $0.38 \leq x \leq 0.52$ (part (e)), and $x > 0.55$ (part (f)). Resistivities lie in the range 1–3 kΩ cm, 1 Ω cm–600 Ω cm, and 0.002–0.02 Ω cm for regimes *(i)*, *(ii)*, and *(iii)* respectively. Seebeck coefficients peak at 60–120 μV/deg and 10–30 μV deg for regimes *(i)* and *(ii)* respectively; they fall in the range −2 to −8 μV/deg in regime *(iii)*.

ated at slightly lower energies and is completely filled by electrons at $T = 0$. This disposition is believed to apply to alloys in regimes *(ii)* and *(iii)*. As x is reduced to below $x_c \approx 0.3$, the $3d_g$ band continually narrows because the orbital overlap diminishes, since the $3p\sigma$ orbitals have a much smaller radial extension than the $4p\sigma$ orbitals. Below a certain critical band width, the central peak disappears, leaving only the two Hubbard subbands. The lower portion, $3d_g$, is completely filled and upper half, $3d_g^*$, empty, as depicted in Fig. 2(b). This situation is believed to apply to alloys in regime *(i)*.

On the basis of Fig. 2(b), NiS_2 and $NiS_{2-x}Se_x$ with $x \leq 0.3$ are insulators at $T = 0$. As T is increased these compounds become intrinsic semiconductors through the thermal promotion of charge carriers across the energy gap. This rationalizes the exponential decline of ρ with rising T. Furthermore, the Seebeck coefficient of an intrinsic semiconductor is specified

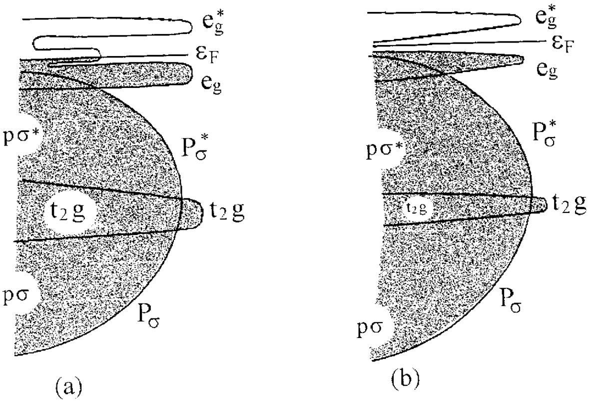

Fig. 2. Schematic band diagram for the $NiS_{2-x}Se_x$ system. Shaded areas represent occupied energy states. Part (a): Quasimetallic characteristics; Fermi level intersects DOS in midgap region. Part (b): Fermi level falls in gap between upper and lower Hubbard subbands. The top edge of the anionic band falls just slightly below the top edge of the lower Hubbard subband.

by the relation [2]

$$\alpha = \frac{-\sigma_n|\alpha_n| + \sigma_p\alpha_p}{\sigma_n + \sigma_p}\,, \tag{1}$$

where σ_n, σ_p are the partial conductivities of electrons and holes and α_n, α_p are the corresponding Seebeck coefficients. Since the e_g subbands of Fig. 2(b) are very nearly mirror images of each other, the numerator in Eq. (1) approaches zero; this rationalizes the finding that $\alpha \approx 0$ at low temperatures. With rising T a situation is reached where carriers from the top of the much wider $p\sigma$ band at slightly lower energies also begin to be promoted thermally into vacant e_g levels. This generates an increasing density of highly mobile holes in the anionic band, ultimately in sufficient numbers to swamp out the contributions of the charge carriers in the e_g subbands that are of much lower mobility. The electrical resistivity will still be of a thermally activated type. On the other hand, α will first rise after the $p\sigma$ holes become dominant; rather large values of α are reached in the initial stage of the resulting quasi one-carrier semiconductor at low $p\sigma$ hole densities. With rising T the $p\sigma$ hole density increases and α drops correspondingly, as predicted by theory [2]. This rationalizes the observed trend of α with T for regime *(i)*.

A new feature emerges for alloys in category (*ii*). As sketched in Fig. 1(b) these compounds are metallic at low temperature and become semiconductors beyond some critical temperature T_c. This feature is rationalized on the assumption that a gap opens up in the density of states at T_c.

A very simple mechanism for explaining the gap feature was first advanced by Spałek and coworkers [4]; this approach is undoubtedly correct in principle but perhaps not in detail. One compares the thermodynamic properties of essentially localized (ℓ) charge carriers with those in itinerant *(i)* states. In its simplest form we take the energy of the localized set, $E_\ell = 0$, as the zero of energy. The entropy of such carriers is $S_\ell = k_{\rm B} \ln 2$ because each electron can be localized on a lattice site with spin "up" or "down" ($k_{\rm B}$ is Boltzmann's constant). The free energy per carrier is then $F = E - TS = -(k_{\rm B} \ln 2)T$; F changes linearly with temperature, as shown in Fig. 3. On the other hand, for a set of interacting, itinerant free carriers we assume the Sommerfeld law $C_i = \gamma T$ to apply; here γ is related to but different from the free-electron value [4]. One can then determine the energy per particle according to the expression $E_i = \int C dT = E_0 + (1/2)\gamma T^2$ and the entropy per particle according to $S_i = \int (C/T) dT = \gamma T$. The free energy is then given by $F_i = E_i - TS_i = E_0 - (1/2)\gamma T^2$; this quantity varies parabolically with T. These parabolas are sketched in Fig. 3 for different values of the intercept E_0. When E_0 is negative but numerically large, as for curve 1, the parabola always lies below the straight line; then $F_i < F_\ell$ at all T, so that the itinerant state is stable. As E_0 becomes less negative a situation may arise whereby the parabola (curve 3) intersects the straight line at two points. Then for $T < T_{3\ell}$ or $T > T_{3u}$, $F_i < F_\ell$, but in the range $T_{3\ell} < T < T_{3u}$, $F_\ell < F_i$. This corresponds to the case of reentrant metallic behavior — as in Cr-doped V_2O_3. For E_0 values that are even less negative, as in curve 4, the itinerant state is encountered in the low temperature range $T < T_4$, and the localized configuration applies for $T > T_4$. This rationalizes regime *(ii)* for $NiS_{2-x}Se_x$, or more generally, for the case of a material that is metallic at low temperatures and becomes an insulator at higher temperatures. Finally, for $E_0 > 0$ one finds, according to curve 2, that $F_\ell < F_i$ at temperatures $T < T_2$; the system switches to the metallic state for $T > T_2$; this is the more commonly encountered insulator-metal transition.

The value of E_0 is clearly crucial in determining the characteristics of the interacting electron system. This quantity is specified by [4]

$$E_0 = -\Phi(\eta)|\bar{\varepsilon}| + U\eta \,. \tag{2}$$

In the absence of electron interactions, $E_0 = -|\bar{\varepsilon}|$ involves the average value of the energy for all electrons in the conduction band (*e.g.* for a half-filled rectangular band of width W, $\bar{\varepsilon} = -W/4$). In the Hubbard approximation the electrons are also subject to an intra-atomic repulsion energy U when two of them temporarily reside on the same site with paired spins. Let the probability of double occupation of a given site be η; then $+U\eta$ is the potential energy of interaction per electron pair. Next, to simulate the increasing difficulty of getting interacting mobile electrons to move past each other, Spałek and coworkers [4] introduced a band narrowing factor $\Phi(\eta)$; η and $\Phi(\eta)$ are specified in terms of U and W by the theory; their exact form need not concern us here.

Eq. (2) shows that E_0 is governed by the balance between the kinetic energy $-\Phi(\eta)|\bar{\varepsilon}|$ that is negative relative to the zero of energy for localized carriers, and by the potential energy of interactions $U\eta$ that is positive. For alloys in category *(ii)* the kinetic contribution evidently slightly outweighs the potential energy (*cf.* curve 4 of Fig. 3); this explains the qualitative features of Fig. 1(b). As concerns the Seebeck coefficients, the e_g bands in regime *(ii)* are wider than those of regime *(i)*, so that the disparity in mobility is now smaller than for case *(i)*; hence, the peak in α is now smaller than before.

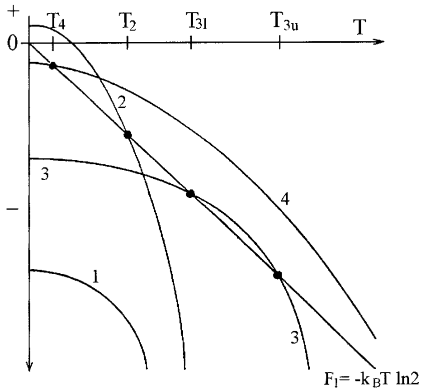

Fig. 3. Free energy curves for localized (ℓ) and itinerant *(i)* electrons in a half-filled, nondegenerate band. See text for details.

Finally, the characteristics of regime *(iii)* may be explained by noting that the central DOS peak of Fig. 2(a) is now sufficiently developed so that the Fermi level always lies within a narrow band. The material is a poor metal, with electrical characteristics as schematically depicted in Figs. 1(c) and 1(f). One sees then how the electrical properties of $\mathrm{NiS}_{2-x}\mathrm{Se}_x$ can be fine tuned by adjustment of x.

2. Critical phenomena in electrical properties of $\mathrm{NiS}_{2-x}\mathrm{Se}_x$

We next turn to another avenue of investigation. This consists in adjusting x so that the alloy is insulating but very close to the borderline between insulator and metal. The compound is subsequently rendered slightly metallic by application of hydrostatic pressure under conditions where quantum critical fluctuations become manifest. The $\mathrm{NiS}_{2-x}\mathrm{Se}_x$ system is thus a good medium for studies of critical phenomena in the electrical properties of solids:

specifically, the resistivity was measured by Rosenbaum and collaborators [5] as a function of temperature $T < 1$ K at a set of different pressures P slightly in excess of the critical pressure $P_\mathrm{c} = 1.51, 1.67$ kbar (depending on the exact sample composition), or as a function of pressures $P > P_\mathrm{c}$ at a fixed temperature $T = 50$ mK. The elucidation of such properties requires a digression (necessarily brief and superficial here) into scaling theories; see *e.g.* Ref. [6,7] for a proper and readable discussion of this topic.

These are based on the classic thermodynamic principle of homogeneity, as illustrated by the volume V of a system containing n_i moles of species i; $V = V(n_1, n_2, \ldots, n_i, \ldots)$. At constant T and P let the system now be altered to contain λn_i moles for each species i. Then the volume obeys the condition $V(\lambda n_1, \lambda n_2, \ldots, \lambda n_i, \ldots) = \lambda V$ (*e.g.*, if the number of moles of each constituent is doubled the volume doubles). This concept must now be generalized. Taking the Gibbs free energy density g as an example it is supposed that for a system close to a critical pressure P_c and critical temperature T_c, g should depend on the independent variables $\bar{p} \equiv (P - P_\mathrm{c})/P_\mathrm{c}$ and $\bar{t} \equiv (T - T_\mathrm{c})/T_\mathrm{c}$ according to [6]

$$g(\lambda^{\xi_t}\bar{t}, \lambda^{\xi_p}\bar{p}) = \lambda g(\bar{t}, \bar{p}) \,, \tag{3}$$

where ξ_p, ξ_t are exponents that must be empirically determined. Eq. (3) is to hold for any arbitrary assignment of λ. To make contact with experiment we set $\lambda = (-\bar{t})^{1/\xi_t}$; *i.e.* $\lambda^{\xi_t} = (-\bar{t})$, and differentiate g with respect to $\bar{p}$ at fixed $\bar{t}$; this generates a molar volume v as follows:

$$\lambda^{\xi_p} \frac{\partial g(\lambda^{\xi_t}\bar{t}, \lambda^{\xi_p}\bar{p})}{\partial(\lambda^{\xi_p}\bar{p})} = \lambda \frac{\partial g(\bar{t}, \bar{p})}{\partial \bar{p}} \,, \tag{4}$$

or

$$v(\bar{t}, 1) = (-\bar{t})^{(1-\xi_p)/\xi_t} v(-1, 1) \,. \tag{5}$$

Comparison with experimental measurements near $\bar{t} = 1$ on the variation of v with $P \to P_\mathrm{c}$ then specifies $(1 - \xi_p)/\xi_t$. A similar (double) differentiation process with respect to $\bar{t}$ yields the molar heat capacity C; the corresponding exponent can be checked against experimental changes of C with $T \to T_\mathrm{c}$, so that ξ_p and ξ_t may be obtained separately. The reason for adopting such procedures is that the use of standard equations of state to determine molar volumes and other quantities of interest near the critical point is notoriously unreliable.

More generally, we adopt the hypothesis that a system near its critical point at $T = 0$ is subject to quantum fluctuations that dominate its properties. Let K be a variable under study and let K_c be its critical value. We characterize the measurement of K near K_c by a correlation length ξ, that in turn is linked to $\delta \equiv |K - K_\mathrm{c}|$, the deviation of an experimental variable K from its critical value. One adopts the relation $\xi \sim |\delta|^{-\nu}$, so that as $K \to K_{\mathrm{c}}$, ξ grows indefinitely.

Associated with the above is the time scale that governs the approach to criticality; for, as the correlations length grows, the time scale for establishing the correlation throughout the system also increases. One assumes that the length and time scales (τ) pertaining to criticality are linked by the relation [7]

$$\xi_\tau(K) = \xi^z\,; \quad \xi(K) = |\delta|^{-\nu}, \tag{6}$$

where z is called the dynamic scaling exponent and ν, the correlation length exponent.

The basis for adopting a correlation "length" in the time domain for a quantum system is the following: The partition function is specified through the relation $Z = \mathrm{tr}\,(\exp(-\beta H))$, where H is the appropriate Hamiltonian, $\beta \equiv 1/k_{\mathrm{B}}T$, and tr represents the trace operation. Now $\exp(-\beta H)$ is reminiscent of the time development operator $\exp(-iH\tau/\hbar)$ in the Heisenberg representation. One may link these two factors through the introduction of an imaginary time scale $\tau = -i\hbar\beta$ that is infinite in "length" at $T = 0$, but which has an upper limit $L_\tau = -i\hbar\beta$ for $T > 0$. The establishment of critical length and time scales ξ and ξ_τ is a generic feature of quantum critical phenomena [7].

Accordingly, for a quantum mechanical operator O of interest we postulate that near the critical point (as $K \to K_{\mathrm{c}}$), and for $T = 0$,

$$O(\underset{\sim}{k}, \omega, K) = \xi^{x_\sigma} O(\underset{\sim}{k}\,\xi, \omega\xi_\tau)\,, \tag{7}$$

where $\underset{\sim}{k}$, ω are the momenta (in reciprocal space) and frequency, respectively. The operator on the right now involves dimensionless quantities and is of no direct interest; the effect of K is subsumed though the introduction of the correlation length.

For $T > 0$ we must recall the upper limit L_τ on ξ_τ; because ξ and ξ_τ are linked we also deal with an upper limit $L_\tau^{x_\sigma/z}$ on the correlation length. Accordingly, the scaling form for an operator at $T > 0$ is postulated to be

$$O(\underset{\sim}{k}, \omega, K, T) = L_\tau^{x_\sigma/z} O(\underset{\sim}{k}\, L_\tau^{1/z}, \omega L_\tau, L_\tau/\xi_\tau)\,. \tag{8}$$

Again, the operator on the right involves dimensionless variables and is of no direct interest. This sets up the framework for our subsequent data analysis.

Rosenbaum and collaborators [5] investigated the low temperature resistivities ρ of $\mathrm{NiS}_{2-x}\mathrm{Se}_x$ with $x = 0.44$. Fig. 4 shows that at pressures P well above the critical pressure $P_{\mathrm{c}} = 1.51$ kbar, required to maintain this alloy in

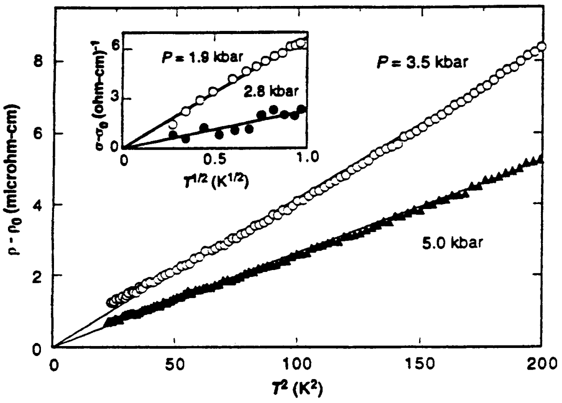

Fig. 4. Resistivity of $NiS_{1.56}Se_{0.44}$ maintained at low temperatures at pressures considerably above $P_c = 1.51$ kbar; note the large T^2 dependence typical of correlated electron systems. Inset shows conductivity in the range $T < 1$ K, where the crystalline disorder gives rise to the observed $\sigma \sim T^{1/2}$ dependence.

the metallic state, $\rho \sim T^2$ in the range 5–14 K; this is consistent with strong electron–electron interactions. The inset to this figure shows that in the very low T range 50–100 mK and for $P \geq 1.9$ kbar, $\rho \sim T^{-1/2}$, consistent with electron scattering in the presence of lattice disorder that then dominates the electrical properties. Fig. 5 shows that when the pressure P is allowed to approach P_c, the conductivity $\sigma \sim T^{0.22}$, a very unusual value of the exponent. According to Eq. (8) (applicable to resistivities) we must link this exponent to the ratio $L_T^{-x_\sigma/z} \sim T^{x_\sigma/z}$ (applicable to conductivities); thus, $x_\sigma/z = 0.22$.

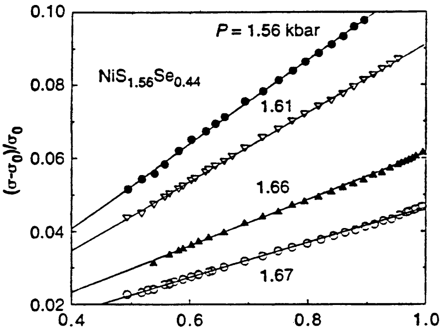

Fig. 5. Dependence of conductivity on temperature for $NiS_{1.56}Se_{0.44}$ maintained at pressure just slightly in excess of P_c; note the $T^{0.22}$ temperature dependence.

In a second set of experiments [5] these workers measured the variation of σ with $\bar{p}$ at $T = 50$ mK. This is sufficiently close to $T = 0$ to permit use of Eq. (7). With $\xi^{x_\sigma} \sim |\delta|^{x_\sigma^\nu} \sim \bar{p}^{x_\sigma^\nu} \equiv \bar{p}^\mu$ and from the data of Fig. 6 one deduces that $\sigma \sim \bar{p}^\mu$, with $\mu = 1.1 \pm 0.2$. Then, according to the data of Fig. 5, $x_\sigma/z = \mu/z\nu = 0.22 \pm 0.02$, so that $z\nu \approx 4.6$.

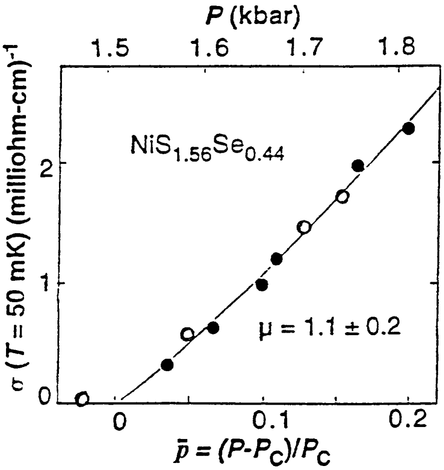

Fig. 6. Conductivity of $\mathrm{NiS_{1.56}Se_{0.44}}$ at 50 mK as a function of the ratio $(P - P_c)/P_c$. Open and closed circles represent two samples with slightly different P_c values.

To test the overall consistency of this approach one notes that the ratio of the measurements $\sigma(\bar{p}, \bar{t})$ and $\bar{p}^\mu$ should follow the relation

$$\frac{\sigma}{\bar{p}^\mu} \sim \frac{\bar{t}^{x_\sigma/z}}{\bar{p}^{x_\sigma \nu}} \sim \left(\frac{T^{1/z}}{p^\nu}\right)^{x_\sigma} . \tag{9}$$

On taking logarithms one finds that a plot of $\ln(\sigma/\bar{p}^\mu)$ *vs* $\ln(T/\bar{p}^{z\nu})$ should produce a universal curve. Indeed, as Fig. 7 shows, the data taken at various $\bar{p}$ do collapse onto a single plot (the slight kink in the graph is not presently understood). This is proof that the scaling procedure outlined above is applicable to the present experimental data.

One can separate out z from ν by additional conductivity studies in the non-ohmic regime. The relevant analysis is based on the use of ℓ_ε, the mean free path, as the dominant length scale of the experiment near the critical point, with a corresponding time scale ℓ_ε^z. The electronic contribution to the field $\mathcal{E}$ is associated with the energy change $E = e\mathcal{E}\ell_\varepsilon$; by the uncertainty principle we also posit that $\Delta E = \hbar/\xi_\tau \sim \ell_\varepsilon^{-z}$, so that $\ell_\varepsilon^{z+1} \sim \mathcal{E}^{-1}$, or $\ell_\varepsilon \sim \mathcal{E}^{-1/(1+z)}$. One defines an effective temperature through the relation

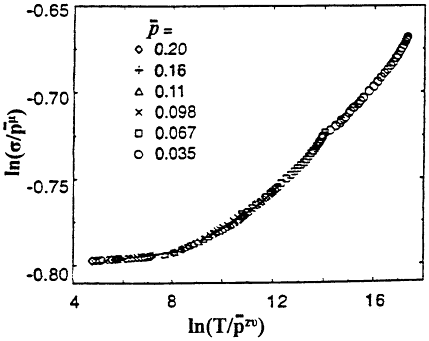

Fig. 7. Collapse of conductivity data in the critical range onto a single curve, as specified by Eq. (9).

$k_B T_{\text{eff}} = e\mathcal{E}\ell_\varepsilon$; this quantity may be found from measurements in the ohmic range. Thus, near the quantum critical point,

$$T_{\text{eff}} \sim \mathcal{E}\ell_\varepsilon \sim \mathcal{E}^{z/(1+z)} . \tag{10}$$

A plot of $\log T_{\text{eff}}$ *vs* $\log \mathcal{E}$ should then yield a single curve whose slope is given by $z/(1+z)$. Experiments [5] indeed display the predicted universality, as shown by the representative data of Fig. 8 for $P = 1.56$ kbar and for $0.35 \le T \le 0.80$ K. Similar results were obtained for $P = 1.51$ and 1.70 kbar. From the observed slope one obtains a value of $z = 2.7 \pm 0.35$, whence $\nu = 1.7 \pm 0.25$, and $x_\sigma = 0.64 \pm 0.13$.

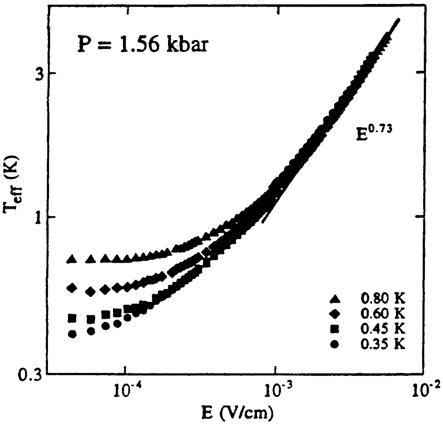

Fig. 8. Effective electron temperature T_{eff} *vs* electric field at $\bar{p} = 0.03$. Note merging of data in the 0.35 to 0.80 K range to a single curve at higher $\mathcal{E}$.

These values have been carefully scrutinized [8] and compared with critical quantum fluctuations observed in other systems. The value $\mu = 1.1$ is consonant with commonly encountered exponents in related systems, but the product z falls outside the generally accepted range. The hyperscaling relation $\mu = (d-2)$ is not satisfied and z falls well outside the expected value of 0.8 to 1. At present there is no consensus in the interpretation of these results. The value of x_σ is particularly puzzling for a system of three dimensions. Further investigations into this problem are therefore warranted.

In any event, the principal aim so far has been to show the great versatility of the $NiS_{2-x}Se_x$ system: by varying x one can achieve gradations in electrical characteristics that probe electron correlation effects. Furthermore, for properly chosen x one can study the characteristics of the system in the region of quantum critical phenomena.

3. Correlations in the V_2O_3 system

We next turn to several manifestations of correlation phenomena in the V_2O_3 system.

The physical characteristics of V_2O_3 and its dilute alloys with neighboring transition metal cations have been studied for a long time; the reader is referred to several reviews [9] for background reading and for references to earlier work. Here we examine recent developments illustrating complexities that must be faced in accounting for the properties of V_2O_3.

Vanadium sesquioxide has generally been regarded as a model system for displaying electron correlation effects. Several experimental properties support this claim: *(i)* The electronic contribution to the low-temperature heat capacity of V_2O_3 — rendered metallic by application of hydrostatic pressure, or by incorporation of 1–5 at % Ti, or by incorporation of excess oxygen — is exceptionally high in comparison to values for standard metals. *(ii)* The Pauli paramagnetic susceptibility χ in this same group of materials likewise is greatly enhanced over the values associated with a free electron gas. *(iii)* The electrical resistivity ρ of this class of materials at low temperatures T varies as $\rho \sim T^2$; this feature is again characteristic of an interacting electron gas.

Up to now these findings were generally interpreted in terms of the Brinkman–Rice (BR) [10] theory that deals with interacting electrons occupying a single nondegenerate band; in light of more recent work this model has to be altered, as described earlier, in conformity with Ref. [3]. For present purposes we begin by using the elementary models of Ref. [4], summarized earlier, to indicate how electron correlations give rise to metal insulator transitions or to reentrant metallic behavior. This rationalizes [11] the observed successive transitions in V_2O_3 with rising temperature T between the antiferromagnetic insulating (AFI), Paramagnetic Metallic (PM), and Paramagnetic Insulating (PI) states [12], shown in the phase diagram of Fig. 9. One should note that through Cr doping one moves towards the right, whereas by application of pressure, Ti doping, or by increasing V vacancies one moves to the left of the diagram. However, factors other than electron correlations are also involved in these transitions: first, even though the PM–PI transformation involves no change in lattice symmetry the transition is accompanied by enormous hysteresis effects, of the order of 50–70 K. This clearly shows that even in the simplest of the three transitions one should not ignore the role of the lattice. Second, in the PM–AFI transition most of the observed entropy change (based on heat capacity measurements) can be accounted for by use of the standard $\Delta S = R\ln(2J+1)$ expression. This indicates that magnetic ordering plays an important role in this particular transformation. A variety of additional mechanisms listed in Ref. [12] have also been invoked to explain the various phase transitions in the V_2O_3 system, though many of these are probably irrelevant in the present case.

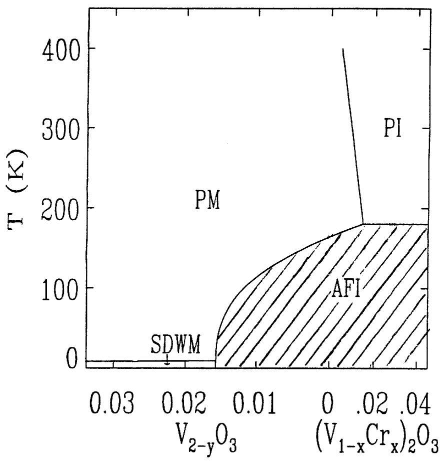

Fig. 9. Phase diagram of the V_2O_3 system, determined as a function of composition. PM — paramagnetic metal, PI — paramagnetic insulator, AFI — antiferromagnetic insulator, SDW — spin density wave in an antiferromagnetic metal (AFM). Hatched region corresponds to the only phase in which antiferromagntic ordering of the type shown in Fig. 11(b) is encountered.

The phase diagram, Fig. 9, is somewhat misleading, in that one cannot superficially equate the effects of pressure, of doping with Ti, or of introducing cation defects by use of excess oxygen. This is brought out in Fig. 10, where the electronic heat capacity γ is shown as a function of pressure P, or as the deviation y in $V_{2-y}O_3$ from perfect stoichiometry [13]. One sees that as the pressure is reduced towards the critical value P_c, below which V_2O_3 enters the insulating phase, the heat capacity rises indefinitely, essentially in accord with the BR theory: $\gamma = \gamma_0/(1-I)^2$, $I \equiv U/U_c$, where γ_0 is the value in the absence of electron correlation effects, U is the Hubbard one-site Coulomb repulsion energy between two electrons, and U_c is its critical value. This should be contrasted with the effect of decreasing the degree of nonstoichiometry y towards its critical value y_c that separates the metallic from the insulating state. In these particular experiments γ is only slightly reduced in value. The difference in these properties arises from the fact that with reduced pressure the band width narrows, thus increasing U, whereas changes in y reflect alterations in the degree of filling of the conduction band of nearly constant width.

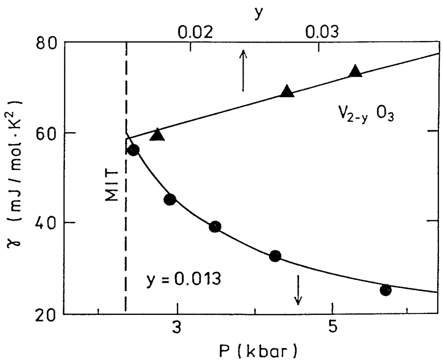

Fig. 10. Electronic contribution to the heat capacity as a function of applied hydrostatic pressure and cation vacancy concentration. The vertical dashed line represents the boundary between the metallic (right) and insulating (left) states.

We next draw attention to one more phase shown in Fig. 9. On cooling the PM phase one encounters near 10 K a transition to an antiferromagnetic metallic (AFM or SDWM) configuration whose magnetic structure was recently determined [14], as shown in Fig. 11(a): The spins lie in the basal planes of the corundum structure and form a honeycomb pattern. When stacked vertically along the c axis the spins form a left- or right-handed spiral pattern with a pitch of nearly $3\pi/2$. This arrangement is to be contrasted with the very different spin configuration of Fig. 11(b) for the AFI phase, as determined by Moon [15]. Here the spins are canted by 71° away from the c axis; they are arranged ferromagnetically within a given vertical slab, with successive parallel slabs showing opposite spin orientations.

The discussion points up that the AFI arrangement is encountered only in the hatched region of the phase diagram of Fig. 9; outside this range the

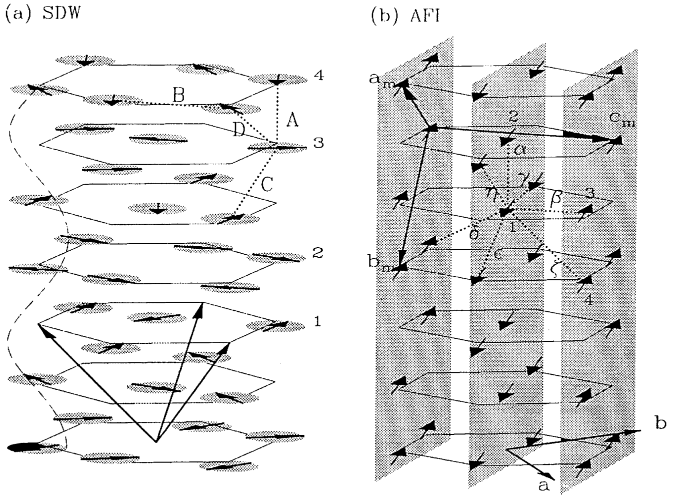

Fig. 11. Magnetic ordering in the AFM–SDW V_2O_3 phase (part (a)) and in the AFI phase (part (b)).

spin spiral arrangement prevails in the AFM–SDW region, and remnants at this type of ordering are also encountered both in the PM and in the PI portions of the phase diagram. More precisely, the elastic sharp magnetic neutron diffraction peaks centered on (1,0,0.3) and (1,0,2.3) in the AFM (SDW) phase give way to very broad magnetic inelastic scattering peaks characterizing the PM and PI phase. This is best illustrated by reference to Figs. 12 and 13, where various types of diffraction peaks are shown. Fig. 12 pertains to diffraction peaks observed for V_2O_3 whose low temperature state ($T < 140$ K) is the AFI configuration; as indicated by the solid circles, the inelastic scattering peaks occur at $(^1/_2,^1/_2,\ell)$, with no noticeable diffraction intensity along $(1,0,\ell)$. When V_2O_3 is heated to 200 K where the PM phase prevails (open circles), the situation is reversed; now the diffraction peaks are encountered along $(1,0,\ell)$, with no noticeable intensity along $(^1/_2,^1/_2,\ell)$. Thus the system switches from magnetic ordering for the AFI phase to a quite distinctive ordering in the PM phase, reminiscent of the ordering in the AFM (SDW) state. A rather similar situation is shown for Fig. 13 displaying data for $V_{1.94}Cr_{0.06}O_3$, that, on raising the temperature, switches from the AFI to the PI phase. Thus, the magnetic ordering pattern changes completely on exiting the AFI phase to any of the other phases of the V_2O_3 system.

The intensity patterns for the PM phase have been rationalized on the basis of the self consistent renormalization (SCR) theory of Moriya [16] in the small magnetic moment limit. By standard methodology one uses measured inelastic diffraction peak intensities to obtain the imaginary component χ''

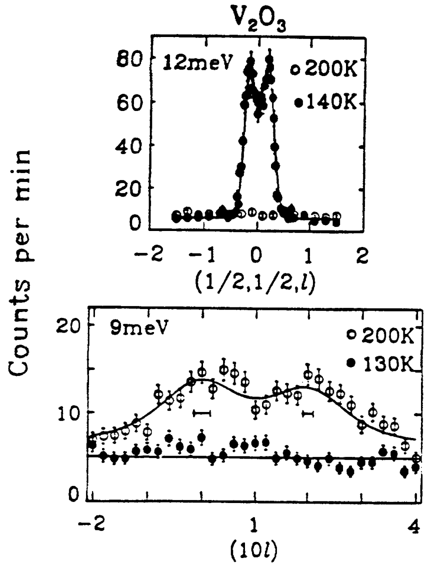

Fig. 12. Constant energy scans along ($^1/_2$,$^1/_2$,ℓ) (upper panel) and (1,0,ℓ) (lower panel) in the PM (open circles) and AFI (solid circles) phases of V_2O_3.

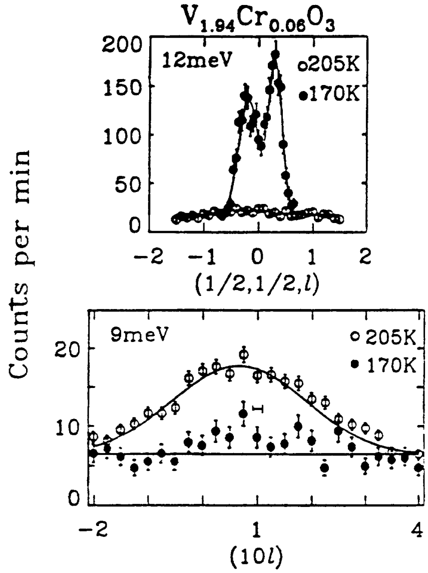

Fig. 13. Constant energy scans along ($^1/_2$,$^1/_2$,ℓ) (upper panel) and (1,0,ℓ) (lower panel) in the PI (open circles) and AFI (solid circles) phases of $V_{1.94}Cr_{0.06}O_3$.

of the magnetic susceptibility. In the relevant SCR scheme this quantity is specified by

$$\frac{\chi''(Q+\underset{\sim}{q},\omega)}{\chi_Q} = \frac{1}{1+\left(\frac{q}{\kappa}\right)^2}\,\frac{\hbar\omega\gamma_A\left(\kappa^2+q^2\right)}{(\hbar\omega)^2+\left[\gamma_A\left(\kappa^2+q^2\right)\right]^2}, \tag{11}$$

where γ_A is a temperature-independent parameter, $\underset{\sim}{q}$ is the displacement from the antiferromagnetic Bragg vector $\underset{\sim}{Q}$, κ is the inverse correlation length $\xi^{-1}, \hbar\omega$ is the energy transfer, and χ_Q is the staggered magnetic susceptibility.

Representative intensity *vs* q plots based on Eq. (11) are shown in Fig. 14 for $\hbar\omega = 3$ meV at a variety of temperatures, using the data displayed in Fig. 15 as input parameters. Note that the maximum value of the intensity at $q = 0$ remains finite; no resonances occur. This is a reflection of the proximity of the system to the critical quantum fluctuation regime.

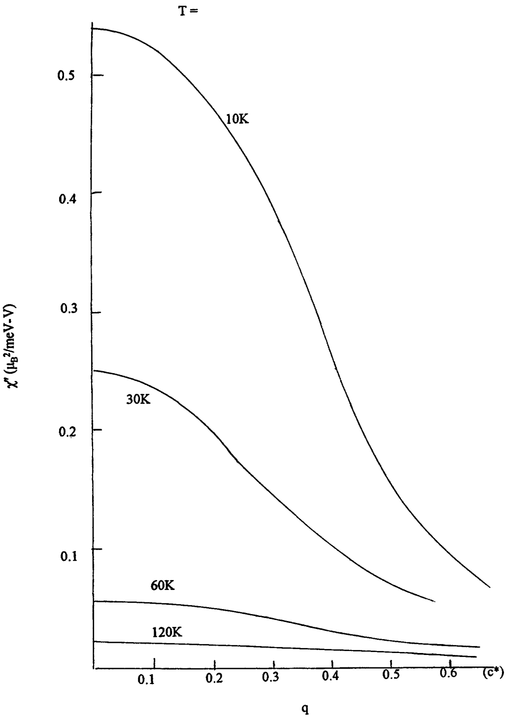

Fig. 14. Plots of χ'' *vs* q for $\hbar\omega = 3$ meV, as determined according to Eq. (11), using the data of Fig. 15 as input parameters.

The values of the parameters of Eq. (11) for V_2O_3 are shown in Fig. 15 as a function of temperature T. The staggered susceptibility follows the Curie–Weiss law over a considerable temperature range. Note that at higher T the correlation length ξ barely exceeds the interionic distances in V_2O_3 and that ξ is smaller in the PI than in the PM phase.

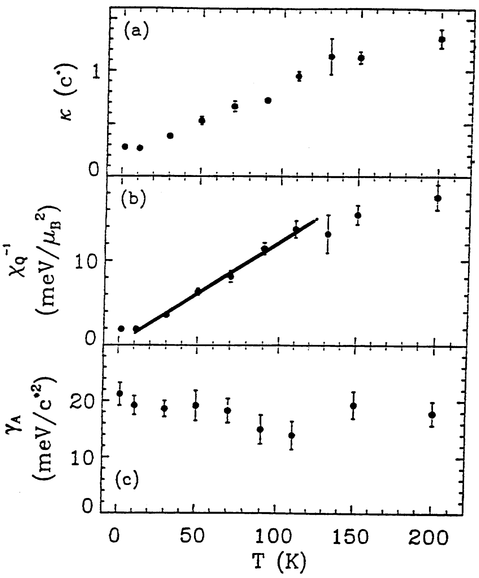

Fig. 15. Variation of input parameters $\kappa, \chi_Q^{-1}, \gamma_A$ as a function of temperature; $c^* = 0.448$ Å^{-1} in the AFM phase.

The change in magnetic ordering in passing from the AFI to the various other phases requires an explanation that goes beyond the one band approximation. Two views have recently been advanced. In the model adopted by Sawatzky and coworkers [17] the two electrons of the Vd^2 ion configuration are distributed with comparable probability among the energetically lower lying a_1 state and on one of the doubly degenerate e states. The net spin then is $S = 1$ per V atom, as compared to the experimental magnetic moment of 1.2 Bohr magnetons. The workers of Ref. [17] justify adoption of this model through the comparison of their measured V $L_{2,3}$ X-ray absorption intensities, taken with the electric vector $E||c$ and $E \perp c$, with differences calculated on applying LDA + U theory to a VO_6 cluster. If the a_1 state were projected out, as described below, the calculation would disagree with experiment. Based on their work the authors determined that on average for the two electrons per V atom, the ratios of the e/e *vs* e/a_1 occupancy is 2 : 1 for the AFI phase, 1 : 1 for the PM phase, and 3 : 2 for the PI phase.

An alternative treatment of this problem was developed earlier, based on qualitative arguments advanced by Goodenough [18] and on a more rigorous assessment by the Ranninger group [19] over 20 years ago. In this approach it is recognized that there exist V–V molecular-like units along the c axis of the PI corundum phase. On entering the monoclinic AFI configuration the internuclear axis tilts away from the c axis, and the two V atoms of the molecular unit move slightly apart. In accord with chemical intuition, the two electrons occupying the lowest-lying a_1 state on the two paired V atoms are deemed to form a covalent bond, so that the a_1 states may be projected out. In this view the V–V pairing is the result of chemical bonding rather than deriving from the ionic configuration of the corundum lattice. The remaining electron on each V atom in the lattice then occupies the e state, with a resultant net spin of $S = {}^1\!/_2$.

Ranninger and coworkers considered various alternative configurations for the remaining e-state electron that can occupy either of the two degenerate e states on different V atoms in the same basal plane. This leads to the possibility of bond ordering. They deduced the spin and orbital orderings shown in Fig. 16, as representing the lowest energy state. With the $a_1 \sim 3z^2 - r^2$ orbital removed from further consideration there remain the $d_2 \sim (x^2 - y^2) + (xy)$ and $d_3 \sim (xz) + (yz)$ orbital states. These in turn can be combined into the $r = d_2 + d_3$ and $s = d_2 - d_3$ configurations that are arranged as shown in Fig. 16 as dark and light circles representing V atoms in the cationic sublattice. The arrows represent electron spin alignments. Experimental evidence in favor of this ordered orbital arrangement derives from resonant X-ray absorption measurements [20]: X-ray irradiation at a wavelength centered on the vanadium atomic absorption band impinges on the sample and is absorbed by electrons whose density around the various V atoms is slightly nonspherical. These weakly allowed transitions are monitored as a function of the rotation of the sample around an azimuthal angle; the results are then compared with theoretical predictions. From the overall concordance between theory and experiment the original configuration of the ordered orbitals of Ref. [14] was adopted by these workers.

As Fig. 16 suggests, the orbital and spin coordinates are very closely interlinked; these degrees of freedom must therefore also be closely coupled in the relevant Hamiltonian, as discussed by Kugel' and Khomskii [21], and as adapted by Rice [22] to the case of V_2O_3. On exiting the AFI phase the orbital ordering is severely perturbed; this leads to the scrambling of the spin configuration as well, as discussed by Rice [22] and by Bao and coworkers [14].

At present the issue as to whether the $S = 1$ or $S = {}^1\!/_2$ model is appropriate to the ordered magnetic insulating phase of V_2O_3 has not been settled.

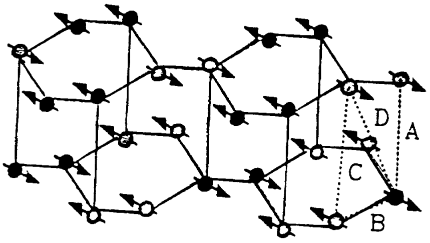

Fig. 16. Proposed orbital ordering in the AFI phase of V_2O_3, see Refs. [14,22]. The full and empty circles represent V atoms with associated orbitals r and s discussed in the text. The arrows represent electron spin alignments. The oxygen ions are omitted for clarity.

In conclusion, we have surveyed the gradual evolution of the simple BR picture based on considerations of one electron in a nondegenerate band of V_2O_3 to a more sophisticated consideration of two electrons distributed among several accessible d-states. No truly satisfactory picture has emerged at the time of writing, but the trend is very clear: theory and experiment must advance cooperatively to explore the effects of degeneracy that were left out of account in the original assessment, some forty years ago, of electron correlation effects in the V_2O_3 system.

The author wishes to acknowledge his indebtedness to all his collaborators who accumulated the experimental data and provided the appropriate theoretical framework. He is particularly indebted to Prof. G. Sawatzky and Prof. J. Spałek for many illuminating discussions; he is grateful for the hospitality accorded him by the Cracow School of Theoretical Physics. This work was supported on NSF Grant 96-12130-DMR.

REFERENCES

[1] J.M. Honig, J. Spałek, *Chem. Mater.* **10**, 2910 (1998).

[2] T.C. Harman, J.M. Honig, *Thermoelectric and Thermomagnetic Effects and Applications*, McGraw-Hill, New York 1967, Chaps. 3 and 4.

[3] W. Metzner, D. Vollhardt, *Phys. Rev. Lett.* **62**, 324 (1989); M. Jarrel, *Phys. Rev. Lett.* **69**, 168 (1992); A. Georges, W. Krauth, *Phys. Rev. Lett.* **69**, 1240 (1992); X.Y. Zhang, M.J. Rozenberg, G. Kotliar, *Phys. Rev. Lett.* **70**, 1666 (1993); M.J. Rosenberg, G. Kotliar, X.Y. Zhang, *Phys. Rev.* **B49**, 10181 (1994).

[4] J. Spałek, A.M. Oleś, J.M. Honig, *Phys. Rev.* **B28**, 6802 (1983); J. Spałek, J.M. Honig, M. Acquarone, A. Datta, *J. Magn. Magn. Mat.* **54–57**, 1047 (1988); J. Spałek, A. Datta, J.M. Honig, *Phys. Rev. Lett.* **59**, 728 (1987).

[5] A. Husmann, D.S. Jin, Y.Z. Zastavker, T.F. Rosenbaum, X. Yao, J.M. Honig, *Science* **274**, 1874 (1996); A. Husmann, J. Brooke, T.F. Rosenbaum, X. Yao, J.M. Honig, *Phys. Rev. Lett.* **84**, 2465 (2000).

[6] H.E. Stanley, *Introduction to Phase Transitions and Critical Phenomena*, Clarendon Press, Oxford 1971.

[7] S.L. Sondhi, S.M. Girvin, J.P. Carini, D. Shahar, *Rev. Mod. Phys.* **69**, 315 (1997).

[8] E. Abrahams, G. Kotliar, *Science* **274**, 1853 (1996); J.C. Phillips, *Proc. Natl. Acad. Sci.* USA **94**, 10532 (1997); A.M.J. Schakel in *Correlations, Coherence, and Order*, eds D.N. Shopova and D.I. Uzunov, Plenum, New York 1999, p. 205ff; A.M.J. Schakel, *J. Phys. Studies* **3**, 337 (1999).

[9] J.M. Honig, L.L. Von Zandt, *Ann. Rev. Mater. Sci.* **5**, 225 (1975); N.F. Mott in *Festkoerperprobleme* Vol. 19, Vieweg, Braunschweig 1979, pp. 331ff; J.M. Honig, *J. Solid State Chem.* **45**, 1 (1982); N.F. Mott, *Metal Insulator Transisions*, second edition, Taylor & Francis, London 1990; M. Yethiraj, J.M. Honig in *Advances in Synthesis and Reactivity of Solids*, Vol. 2 ed. T.E. Mallouk, JAI Press, London 1994, pp. 235ff; M. Yethiraj, *J. Solid State Chem.* **88**, 53 (1990).

[10] W.F. Brinkman, T.M. Rice, *Phys. Rev.* **B2**, 4302 (1971).

[11] J. Spałek, *J. Solid State Chem.* **88**, 70 (1990).

[12] H. Kuwamoto, J.M. Honig, J. Appel, *Phys. Rev.* **B22**, 2626 (1980).

[13] S.A. Carter, T.F. Rosenbaum, P. Metcalf, J.M. Honig, J. Spałek, *Phys. Rev.* **B48**, 16841 (1993).

[14] W. Bao, C. Broholm, S.A. Carter, T.F. Rosenbaum, G. Aeppli, S.F. Trevino, P. Metcalf, J.M. Honig, J. Spałek, *Phys. Rev. Lett.* **71**, 766 (1993); W. Bao, C. Broholm, J.M. Honig, P. Metcalf, S.F. Trevino, *Phys. Rev.* **B54**, R3726 (1996); W. Bao, C. Broholm, G. Aeppli, P. Dai, J.M. Honig, P. Metcalf, *Phys. Rev. Lett.* **78**, 507 (1997); W. Bao, C. Broholm, G. Aeppli, S.A. Carter, P. Dai, C.D. Frost, J.M. Honig, P. Metcalf, *J. Magn. Magn. Mater.* **177-181**, 283 (1998).

[15] R.M. Moon, *Phys. Rev. Lett.* **25**, 527 (1970).

[16] H. Hasegawa, T. Moriya, *J. Phys. Soc. Jpn.* **36**, 1542 (1974); K. Nakayama T. Moriya, *J. Phys. Soc. Jpn.* **56**, 2918 (1987).

[17] J.-H. Park, L.H. Tjeng, A. Tanaka, J.W. Allen, C.J. Chen, P. Metcalf, J.M. Honig, F.M.F. deGroot, G.A. Sawatzky, *Phys. Rev.* **B61**, 11506 (2000).

[18] J.B. Goodenough, *Ann. Rev. Mater. Sci.* **1**, 101 (1971); *Progr. Solid State Chem.* **5**, 145 (1971)

[19] C. Castellani, C.B. Natoli, J. Ranninger, *Phys. Rev.* **B18**, 4945, 4967, 5001 (1978).

[20] L. Paolasini, C. Vettier, F. de Bergevin, F. Yakhou, D. Mannix, A. Stunault, W. Neubeck, M. Altarelli, M. Fabrizio, P.A. Metcalf, J.M. Honig, *Phys. Rev. Lett.* **82**, 4719 (1999); M. Fabrizio, M. Altarelli, M. Benfatto, *Phys. Rev. Lett.* **80**, 3400 (1998); *Phys. Rev. Lett.* **81**, E4030 (1998).

[21] K.I. Kugel', D.J. Khomskii, *Sov. Phys. Usp.* **25**, 231 (1982).

[22] T.M. Rice in *Spectroscopy of Mott Insulators and Correlated Metals* Vol. 159, eds A. Fujimori and Y. Takana, Springer, Berlin 1995, pp. 221ff.